RSC Advances

PAPER

View Article Online
View Journal | View Issue

Cite this: *RSC Adv.*, 2017, **7**, 27549

Dielectric, optical and enhanced photocatalytic properties of $CuCrO_2$ nanoparticles

Tokeer Ahmad,*[a] Ruby Phul,[a] Parvez Alam,[a] Irfan H. Lone,[a] Mohd. Shahazad,[a] Jahangeer Ahmed,*[b] Tansir Ahamad[b] and Saad M. Alshehri[bc]

Received 16th November 2016
Accepted 23rd March 2017

DOI: 10.1039/c6ra26888a

rsc.li/rsc-advances

Herein, delafossite $CuCrO_2$ nanoparticles were synthesized through a polymeric citrate precursor method, followed by heating at 900 °C in air. The BET surface area of the $CuCrO_2$ nanoparticles was found to be 235 $m^2\ g^{-1}$, which was more than 500 times that of bulk $CuCrO_2$ (0.47 $m^2\ g^{-1}$) and 2–4 times that of the reported $CuCrO_2$ nanoparticles (50–100 $m^2\ g^{-1}$) (Y.-T. Nien *et al.*, *Mater. Chem. Phys.*, 2016, **179**, 182–188 and D. Xiong *et al.*, *J. Mater. Chem.*, 2012, **22**, 24760–24768). In the photoluminescence spectra of the $CuCrO_2$ nanoparticles, a strong luminescent emission peak was observed at ~460 nm in the blue light region. The resulting transmittance value of the $CuCrO_2$ nanoparticles was found to be 77% in the visible region, and the direct band gap energy was determined to be 3.09 eV *via* UV-vis spectroscopy. The dielectric properties as a function of frequency and temperature and photocatalytic degradation of the organic pollutants in an aqueous solution were also investigated. $CuCrO_2$ nanoparticles also showed remarkable enhancement in the catalytic degradation of methylene blue in H_2O under sunlight irradiation. The plausible fragmentation and the structural changes in the methylene blue molecule were further demonstrated *via* mass spectrometry.

1. Introduction

Nanotechnology has attracted significant interest from many researchers; this is due to the fundamental scientific significance, various applications, and the peculiar and fascinating properties of the nanoparticles, superior to those of the bulk materials.[3] Nanoparticles of transparent conducting oxides have shown a wide range of applications in optoelectronics,[4] photovoltaics,[5] gas sensors,[6] batteries,[7] solar cells, and electrochromic mirrors and windows.[8] Generally, transparent conducting oxides (such as ZnO, SnO_2, TiO_2 *etc.*)[9–11] are n-type materials, but some of them, such as NiO and ABO_2, are p-type delafossite materials, which show significant electrical conductivity due to hole mobility and an optical direct band gap in the visible region.[2,12–18]

Dye-sensitized solar cells (DSSCs) are third-generation photovoltaic devices and have recently gained attention due to their eco-friendly and economical production as compared to conventional photovoltaic devices. The DSSCs fabricated from p-type oxide materials have high surface chemical affinity, large surface area, a wide band gap, desirable valence band potential, and sufficiently high hole mobility.[19] ABO_2 oxides (A = Cu and B = Al, Ga, In, Sc, Y, Cr, rare earths, *etc.*) having delafossite structures with a band gap more than 3.1 eV have been studied as a triangular lattice antiferromagnet prototype with interesting properties, such as transparent conductivity and multiferroicity, and are mostly used in the formation of p-type DSSCs.[20–22] Recently, delafossite $CuCrO_2$ has been investigated due to its higher carrier mobility and positive flat band. In the bulk shape, the direct band gap value of $CuCrO_2$ is found to be 2.95–3.30 eV at room temperature.[23] The nanosized $CuCrO_2$ particles have been used for constructing UV light-emitting diodes,[24] transparent p–n junctions,[25] and photocatalysts for hydrogen evolution,[26] NO_2^- and NO_3^- removal,[27,28] removal of M^{2+} (M = Ni, Cu, Zn, Cd, and Hg),[29] combustion of methane.[30] Recently, delafossite ABO_2 (A = Cu and B = Al, Ga, Fe) nanoparticles were also used as catalysts in H_2–O_2 fuel cell applications[31–33] and in the degradation of bisphenol.[34] Present studies reveal that $CuCrO_2$ nanoparticles could be used as effective photocatalysts in the degradation of organic contaminants in water. A large number of chemical and biological pollutants could be expected in groundwater. Therefore, treatment of polluted water (caused by use or disposal of waste materials in various forms including chemical, agricultural, animal products, industrial waste *etc.*) is the current challenge for scientists to globally control the environmental and unwanted human disease problems.

Delafossite and other nanostructured materials were also synthesized using the acid-catalyzed sol–gel method, ultrasonic process, and hydrothermal and solid state methods.[2,30–33,35–38]

[a]*Nanochemistry Laboratory, Department of Chemistry, Jamia Millia Islamia, New Delhi-110025, India. E-mail: tahmad3@jmi.ac.in*

[b]*Department of Chemistry, College of Science, King Saud University, Riyadh 11451, Saudi Arabia. E-mail: jahmed@ksu.edu.sa*

[c]*Department of Chemistry, College of Science & General Studies, Alfaisal University, Riyadh, Kingdom of Saudi Arabia*

Herein, we report the polymeric citrate precursor synthesis of $CuCrO_2$ nanoparticles (~40 nm) at 900 °C in 12 h in air. Various analytical techniques such as powder X-ray diffraction (XRD), BET surface area analysis, fluorescence spectroscopy, UV-vis spectrophotometry, and transmission electron microscopy (TEM) were used to characterize the $CuCrO_2$ nanoparticles. Dielectric, optoelectronic, and photocatalytic properties of the $CuCrO_2$ nanoparticles were also investigated. Enhanced photocatalytic efficiencies in the degradation of an organic dye (methylene blue) in an aqueous solution were examined for over 150 minutes.

2. Experimental

Ethylene glycol (Spectrochem), citric acid monohydrate (Merck; 99.0%), $CuSO_4 \cdot 5H_2O$ (Merck; >98%), and $Cr(NO_3)_3 \cdot 9H_2O$ (Thomas Baker) were used as received without further purification. All the glassware was thoroughly washed with nitric acid followed by rinsing with deionized water several times before use. Deionized water was used throughout the experiments and in the preparation of stock solutions.

The synthesis of nanoparticles *via* the polymeric citrate precursor route has already been reported in the literature.[39,40] In the present protocol, ethylene glycol (1.4 mL) was mixed with 0.1 M $Cr(NO_3)_3 \cdot 9H_2O$ (25 mL) in a beaker under constant stirring for about 10 minutes at room temperature to obtain a transparent solution. Dried citric acid (21 g) was added to the above mentioned solution in the molar ratio of ethylene glycol : chromium ion : citric acid = 10 : 1 : 40. For the clear solution, the mixture was continuously stirred for about 2 h at room temperature followed by the addition of 0.1 M $CuSO_4 \cdot 5H_2O$ (25 mL) and subsequent stirring for 2 h. The temperature of the above mentioned system was maintained at 55 ± 5 °C for further 2 h to eliminate excess of water and increase the rate of the polyesterification reaction between citric acid and ethylene glycol to obtain the viscous solution. This viscous solution was kept at 135 °C for 20 h in a furnace to vaporize the solvent. A semi-solid product was recovered after polymerization, which was charred for 2 h at 300 °C followed by further heating at 500 °C for 20 h. A black-coloured precursor was obtained, which was used in the synthesis of the $CuCrO_2$ nanoparticles. The synthesized precursor materials were heated at 900 °C for 12 h in an automatic high temperature furnace to obtain nearly green-coloured powder of the $CuCrO_2$ nanoparticles.

The phase analysis and crystallinity of the as-synthesized nanoparticles were determined *via* XRD studies using a Rigaku Ultima IV diffractometer with nickel-filtered Cu-K_α radiation of wavelength 1.5416 Å, and diffraction patterns were obtained in the 2θ range from 20° to 80° with a step size of 0.05° and step time of 1 s. Fourier transform infrared spectra (FT-IR) were obtained *via* an IT Affinity-1, Shimadzu spectrophotometer using KBr discs as a reference. The surface area of the sample was determined *via* a BET (Brunauer–Emmett–Teller) surface area analyser (Quantachrome Instruments Limited, USA, Model Nova 2000e) at liquid nitrogen temperature (77 K) using the multipoint BET method. To remove the water vapour and adsorbed gases from the sample, approximately 0.06 gram of the sample was placed in the sample cell and degassed for 2 h at 200 °C in the vacuum degassing mode. The grain size and morphology of the synthesized nanoparticles were estimated using an FEI Technai G^2 20 transmission electron microscope. The specimens for TEM studies were prepared by deploying a drop of sonicated nanopowder [suspension of powder sample in absolute ethanol for about 15 min using an ultrasonicator (Ultrasonic Processor Model: UP-500)] onto the TEM grid (carbon-coated copper) and drying at 45 °C in an oven for 1 h. Dielectric measurements were carried out *via* a Wayne Kerr high frequency LCR meter (Model: 6505P). Then, 2–3 drops of 5% PVA solution were placed on the fine powder as a fixer agent and dried at 90 °C for 1 h. Finely ground powder was transformed into pellets at a pressure of 3–4 tons, followed by heating of the pellets at 1000 °C for 12 h. Before carrying out the dielectric measurements, the pellets were coated by a silver paste (Ted Pella, Inc.) and dried at 90 °C for 1.5 h to make the surface conducting. Fluorescence studies were carried out using a Perkin-Elmer LS-55 spectrofluorophotometer after dissolving the powders in ethanol. The excitation source was a xenon lamp, and the baseline was corrected before the measurements.

The photocatalytic efficiency of the prepared $CuCrO_2$ nanoparticles was measured against the degradation of methylene blue (MB) under sunlight irradiation. The degradation process was investigated by UV-vis spectrophotometry (Shimadzu, UV-1650) at the maximum absorption wavelength (λ_{max}) of 662.5 nm of MB. Herein, 1 mg of catalyst was dispersed in 50 mL MB (10 mg L^{-1}) and placed in the dark under constant magnetic stirring to obtain the suspension with an adsorption/desorption equilibrium. The degradation process was carried out at room temperature at pH 7. Thereafter, the suspension was subjected to visible light. At 15 min intervals, the sample was obtained and centrifuged at 8000 rpm for 10 min to separate the $CuCrO_2$ nanoparticles, and the transparent solutions were obtained to study the absorption spectra. All the experiments were repeated three times, and the results showed excellent agreement. The degradation rate constants of degraded MB, using the $CuCrO_2$ nanoparticles were calculated using the first-order kinetic reaction as below:

$$\ln\left(\frac{C}{C_0}\right) = -kt$$

where C is the concentration after irradiation, C_0 is the initial concentration, k is the degradation rate constant, and t is time. Mass spectrometry data of the degraded samples was obtained using an AccuTOF LC-plus (JEOL, JMS – T100 LP).

3. Results and discussion

Fig. 1a shows the powder X-ray diffraction (XRD) patterns of the black-coloured precursor and pure $CuCrO_2$ nanoparticles. The black-coloured precursor materials contain a mixture of CuO and Cr_2O_3 at 500 °C (black-coloured line), whereas the pure phase of the $CuCrO_2$ nanoparticles (red-coloured line) was obtained at 900 °C in air (Fig. 1a). The reflections appeared at the 2θ values of 31.43°, 35.22°, 36.42°, 40.90°, 47.95°, 55.90°, 62.41°, 65.60°, 71.56°, and 74.50°, assigned to (006), (101), (012), (104),

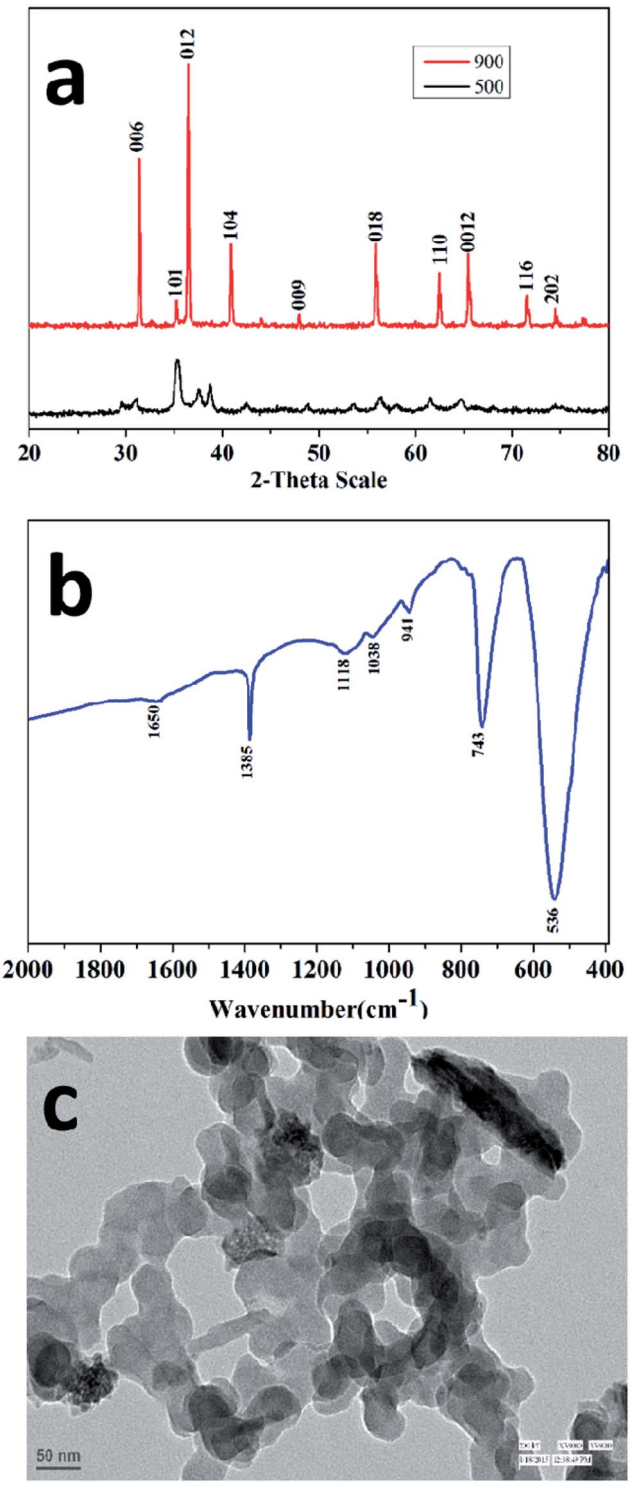

Fig. 1 (a) XRD patterns of the precursor heated at 500 °C in air (black-coloured line) and pure phase of the $CuCrO_2$ nanoparticles obtained at 900 °C and 12 h in air (red-coloured line). (b) FT-IR spectrum and (c) TEM image of the $CuCrO_2$ nanoparticles obtained at 900 °C.

(009), (018), (110), (0012), (116), and (202), in accordance with the JCPDS no. 740983 for the hexagonal crystal structure of $CuCrO_2$. FT-IR spectrum of the $CuCrO_2$ nanoparticles is shown in Fig. 1b. Herein, one weak (~941 cm^{-1}) and two strong bands (~743 and 536 cm^{-1}) could be assigned to the Cr^{III}–O and M–O bond stretching frequencies of the $CuCrO_2$ nanoparticles, respectively.[2,41] The TEM image shows the formation of spherical-shaped $CuCrO_2$ nanoparticles with the average diameter of ~40 nm (Fig. 1c). The agglomerations of the $CuCrO_2$ nanoparticles were also observed to a small extent, which could be due to high temperature (*i.e.* 900 °C) employed in the reactions of the precursors in the synthesis of the $CuCrO_2$ nanoparticles.

The specific surface area of the nanocrystalline $CuCrO_2$ particles was examined through the multipoint BET equation with the relative pressure (P/P_o) in the range from 0.05 to 0.35. The surface area of the $CuCrO_2$ nanoparticles was found to be 235 $m^2\ g^{-1}$, as shown in Fig. 2a. Note that the present surface area of the $CuCrO_2$ nanoparticles is >500 times the surface area of bulk $CuCrO_2$ (0.5 $m^2\ g^{-1}$).[1] Moreover, the surface area of the as-prepared $CuCrO_2$ nanoparticles is 2–4 times that of the previously studied $CuCrO_2$ nanoparticles.[1,2] From the DA plot (Fig. 2b), the pore radius of the $CuCrO_2$ nanoparticles was found to be ~15 nm, which also supported the electron microscopy images. From the TEM data, it is very clear that the particles are spherical in shape with a radius of ~20 nm, which closely matches the particle size obtained from the Dubinin-Astakhov (DA) model.[42]

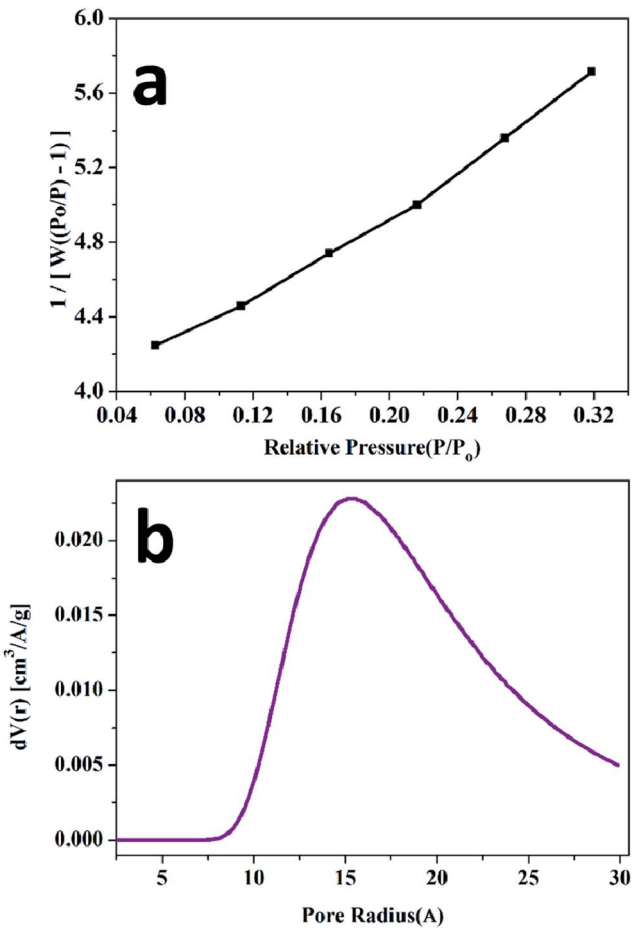

Fig. 2 (a) BET and (b) DA plots of the $CuCrO_2$ nanoparticles.

The dielectric properties of the $CuCrO_2$ nanoparticles were determined as a function of temperature and frequency. Prior to the measurements, the thickness and diameter were calculated to measure the dielectric constant from the measured value of the capacitance. Fig. 3a shows the dependence of the dielectric constant on frequency for the $CuCrO_2$ nanoparticles at different temperatures. The dielectric constant decreases with the increase in frequency due to the inability of the electric dipoles to align with the fast variation of the alternating applied electric field.[43,44] In the low-frequency region, the dielectric constant showed dispersion and achieved a saturation limit at high frequencies. This could be due to the Maxwell–Wagner type interfacial polarization that is in excellent agreement with the Koop's model.[45] Fig. 3b shows the variation of the dielectric loss as a function of frequency at different temperatures. The measurement was carried out in the frequency range from 10 kHz to 1 MHz. The dielectric loss constantly decreases as the frequency increases. Temperature-dependant studies showed that the dielectric constant was maximum at 100 °C, whereas some fluctuations in the dielectric loss were observed at this temperature. The dielectric constant and loss remained nearly stable at 200 °C. Frequency-dependant dielectric loss and dielectric constants of the $CuCrO_2$ nanoparticles are shown in Fig. 3c, which clearly shows that the dielectric properties of the $CuCrO_2$ nanoparticles decrease with the increase in frequency. The decrease in the dielectric constant with the increase in frequency may be associated with the fact that any species contributing to polarization was found to lag behind the applied field at high frequency and hence decreased both properties *i.e.* dielectric constant and dielectric loss.

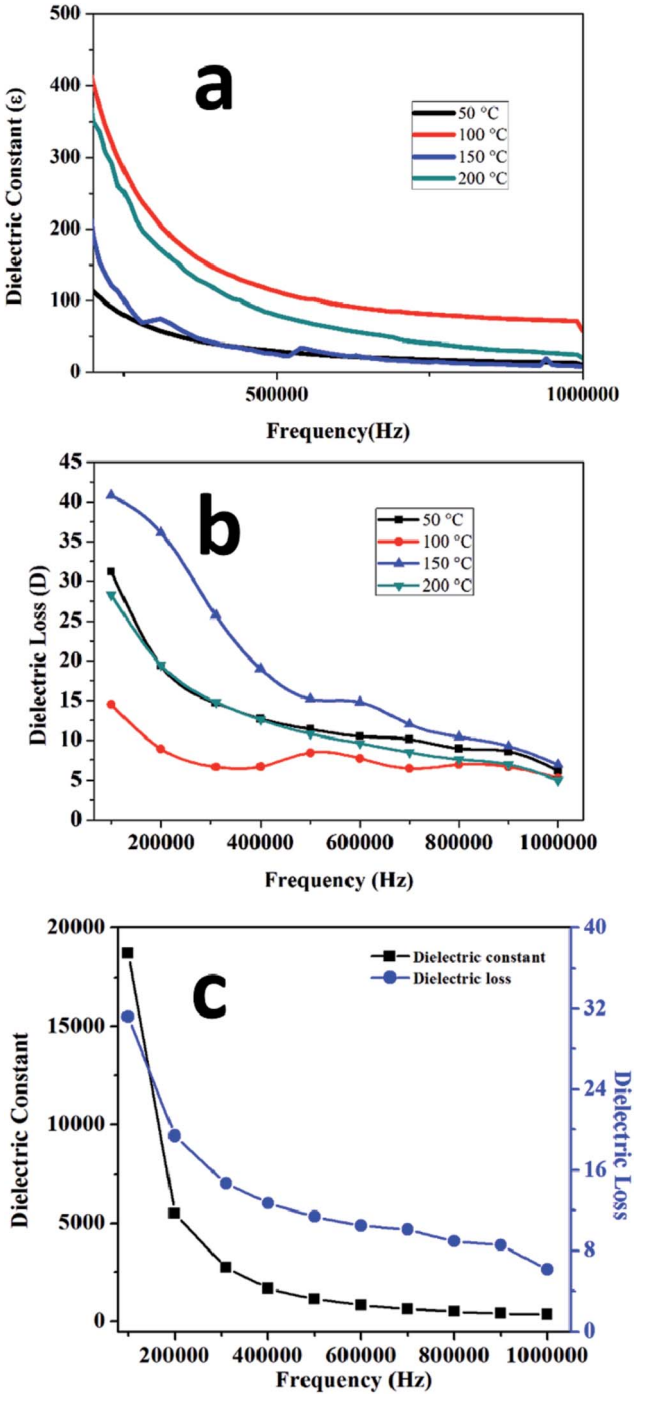

Fig. 3 (a) Dielectric constant and (b) dielectric loss of the $CuCrO_2$ nanoparticles at different temperatures. (c) Variation in the dielectric constant and loss of the $CuCrO_2$ nanoparticles at room temperature as a function of frequency.

Photoluminescence (PL) is a significant technique to study the optical properties of the delafossite materials. Fig. 4 shows the photoluminescence spectra of the $CuCrO_2$ nanoparticles. These nanoparticles show a strong luminescent emission peak at 460 nm in the blue region, and a weak emission peak at 386 nm for an excitation wavelength of 310 nm at room temperature. These transitions could be attributed to the intra-band transitions, implying $3d^9 4s^1$ and $3d^{10}$ in Cu^+ ions, as also reported for other Cu-based delafossite oxide insulators (such as $CuYO_2$ and $CuLaO_2$).[46,47] On comparing $CuCrO_2$ with $CuLaO_2$, it was observed that the luminescence peaks of $CuCrO_2$ shifted towards low energy. This may be a consequence of the interaction of Cu–O with the Cr atom[48] since Cr ion exerts an influence on the Cu–O–Cr–O–Cu linkage owing to more favourable

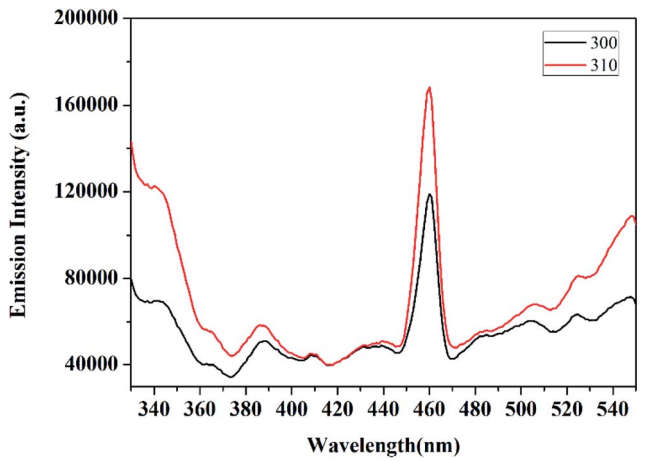

Fig. 4 Photoluminescence (PL) spectra of the $CuCrO_2$ nanoparticles, excited at 300 and 310 nm.

integration of the 3d state on Cr ion, affecting the Cu–O bond length and the Cu–Cu interaction.[49]

Fig. 5 shows the UV-visible spectrum of the $CuCrO_2$ nanoparticles in the range from 200 to 800 nm. The wavelength-dependent transmittance results reveal that the light transmittance value of the $CuCrO_2$ nanoparticles is ~74–80% in the wavelength range from 600 to 800 nm, as shown in Fig. 5a, and the resulting values are found to be higher that the reported values for $CuCrO_2$.[50–52] The photon energy (or band gap energy) of the $CuCrO_2$ nanoparticles was determined using the UV-

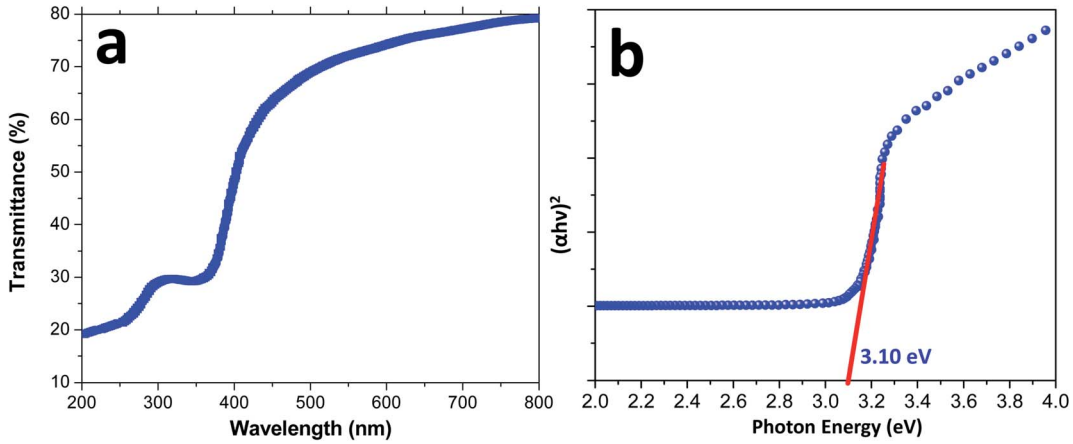

Fig. 5 (a) UV-visible spectrum (wavelength *vs.* percent transmittance) and (b) plot of $(\alpha h\nu)^2$ *versus* photon energy (eV) for the direct band gap determination of the $CuCrO_2$ nanoparticles.

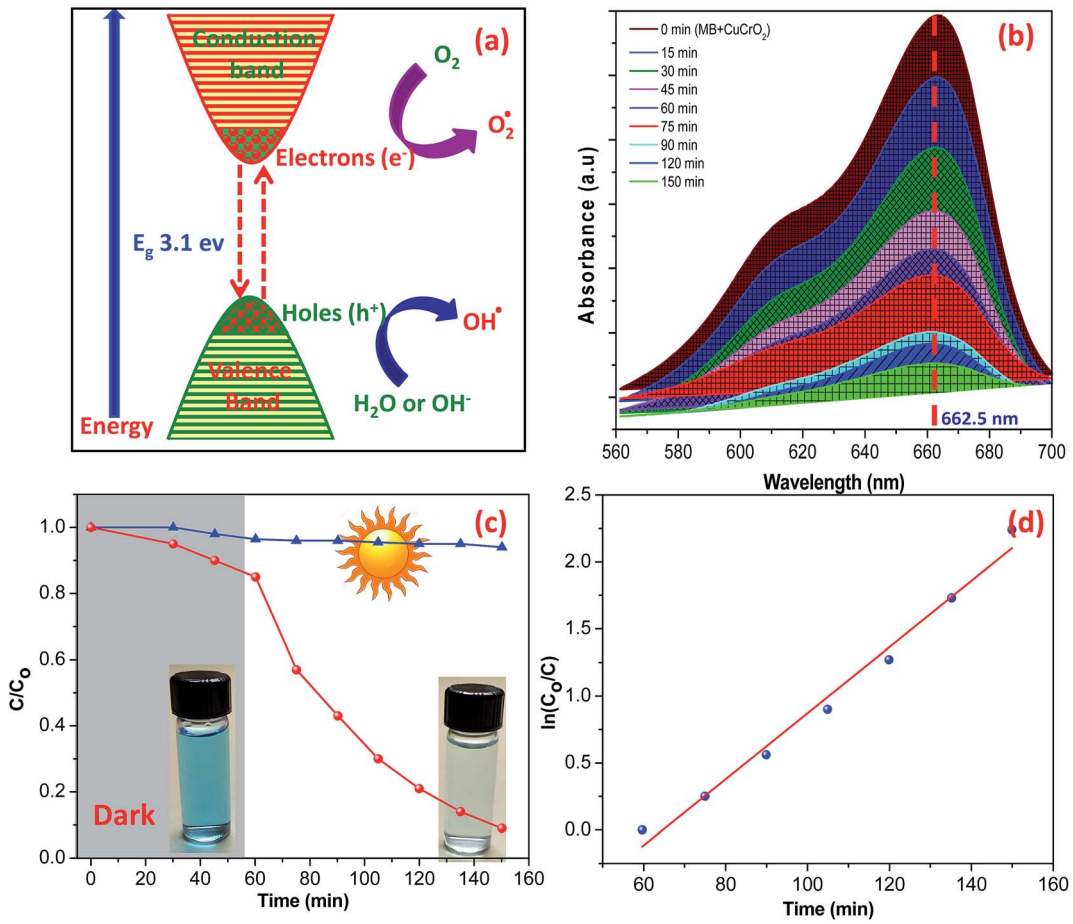

Fig. 6 (a) Schematic of the photocatalytic degradation of MB using $CuCrO_2$ nanoparticles. (b) UV-visible spectra and (c and d) photocatalytic degradation of aqueous MB with time (minutes) under irradiation from sunlight.

visible absorption spectrum of the $CuCrO_2$ nanoparticles. Fig. 5b shows the plot of $(\alpha h\nu)^2$ against photon energy for the $CuCrO_2$ nanoparticles, where α, h, and ν are the absorbance (obtained from UV), Planck's constant, and frequency of the incident beam, respectively. Direct and indirect band gap energies of the solids could be calculated through the Tauc's model.[53,54] Photon energy (intercept of the straight line on the x-axis) demonstrates the direct band gap of the $CuCrO_2$ nanoparticles to be 3.10 eV, which closely matches the reported direct band gap (3.09 eV) of the $CuCrO_2$ thin films.[51] The band gap energies of the materials usually refer to the energy difference between the valence and conduction bands.

The photocatalytic activity of the $CuCrO_2$ nanoparticles was tested in the degradation of MB under irradiation from sunlight for over 150 minutes. The degradation of MB over the $CuCrO_2$ nanoparticles could be explained on the basis of the generation of hydroxyl free radicals ($OH^\bullet$), *i.e.* highly oxidizing agents. When the $CuCrO_2$ nanoparticles were irradiated in sunlight, holes (h^+) were formed in the valence band of the $CuCrO_2$ materials after the excitation of the electrons (e^-) to the conduction band. This could be possible due to the larger energy of sunlight compared to the band gap energy of $CuCrO_2$ (3.1 eV). In an aqueous medium with the presence of oxygen, the holes and electrons produced hydroxyl radicals ($OH^\bullet$) and superoxide radical anions ($O_2^{-\bullet}$), respectively. The hydroxyl radicals ($OH^\bullet$) are strong oxidizing agents and attack the dye molecule to provide the oxidized product, as shown in Fig. 6a and also summarized in the photochemical reactions given below:

$$CuCrO_2 + h\nu \rightarrow CuCrO_2\,(e^- + h^+)$$

$$CuCrO_2\,(h^+) + H_2O \rightarrow CuCrO_2 + OH^\bullet + H^+$$

$$CuCrO_2\,(h^+) + HO^- \rightarrow CuCrO_2 + OH^\bullet$$

In the conduction band, the electrons (e^-) of $CuCrO_2$ reduce molecular oxygen (O_2) to hydroperoxyl radicals (*i.e.* a protonated form of superoxide):

$$CuCrO_2 + O_2 + e^- \rightarrow CuCrO_2 + O_2^{\bullet -}$$

The degradation of the adsorbed compounds (*i.e.* MB) is likely to occur either by the direct oxidation on the surface of the photocatalysts or by hydroxyl radicals:

$$OH^\bullet + MB \rightarrow CO_2 + H_2O \text{ (oxidized products)}$$

The UV-visible spectra of MB in an aqueous solution are presented in Fig. 6b. The distinct characteristic was detected at 662.5 nm, and the absorption band intensity decreased with time under the irradiation of sunlight. The reduction in the intensity of the absorption band of aqueous MB indicates the degradation of dye by UV irradiation over the surface of the $CuCrO_2$ nanoparticles. The degradation efficiencies of MB are shown in Fig. 6c. Note that 79% degradation of MB was observed after 1 h in sunlight, whereas ~16.5% adsorption of MB was observed in the dark for 1 h. Photocatalytic degradation of MB over the surface of pure $CuCrO_2$ nanoparticles (after 1 h) was found to be higher (two to three times) compared to that of the $CuCrO_2/TiO_2$ heterostructures and pure TiO_2, respectively.[55] In parallel, we also performed the experiments in the absence of photocatalysts and found that no degradation of MB occurred in the same time. Fig. 6d shows the linear plots of $\ln(C/C_0)$ *vs.* irradiation time, which support the kinetic data for the degradation of MB. Previously, photocatalytic degradation efficiencies of ~85% and 75% of MB were reported for $CuCrO_2/TiO_2$ heterostructures and pure TiO_2 nanoparticles, respectively, using the comparatively very long irradiation time of 8 h.[55] Note

Table 1 Fragmentations of the MB dye molecule with m/z values (error ± 0.2)

S. no.	Molecule	Observed m/z
1	$C_{16}H_{18}N_3S$	284.54
2	$C_{16}H_{18}ON_3S$	300.54
3	$C_{16}H_{18}O_2N_3S$	316.28
4	$C_{12}H_{10}N_3S$	228.12
5	$C_{13}H_{15}N_2O_3S$	279.16
6	$C_7H_{10}NSO_4$	205.05
7	$C_6H_8NSO_4$	192.13
8	$C_8H_9NO_3$	167.13
9	$C_6H_{10}NO_4$	161.09

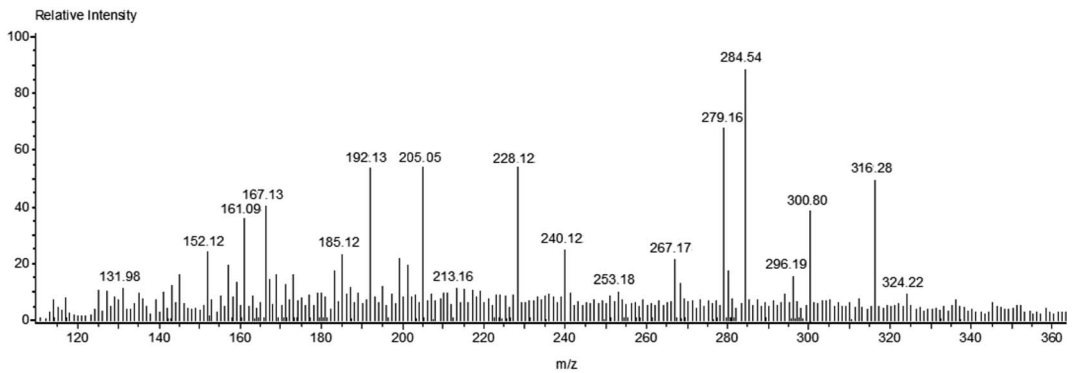

Fig. 7 Mass spectrum of MB dye after 60 minutes of photodegradation reaction.

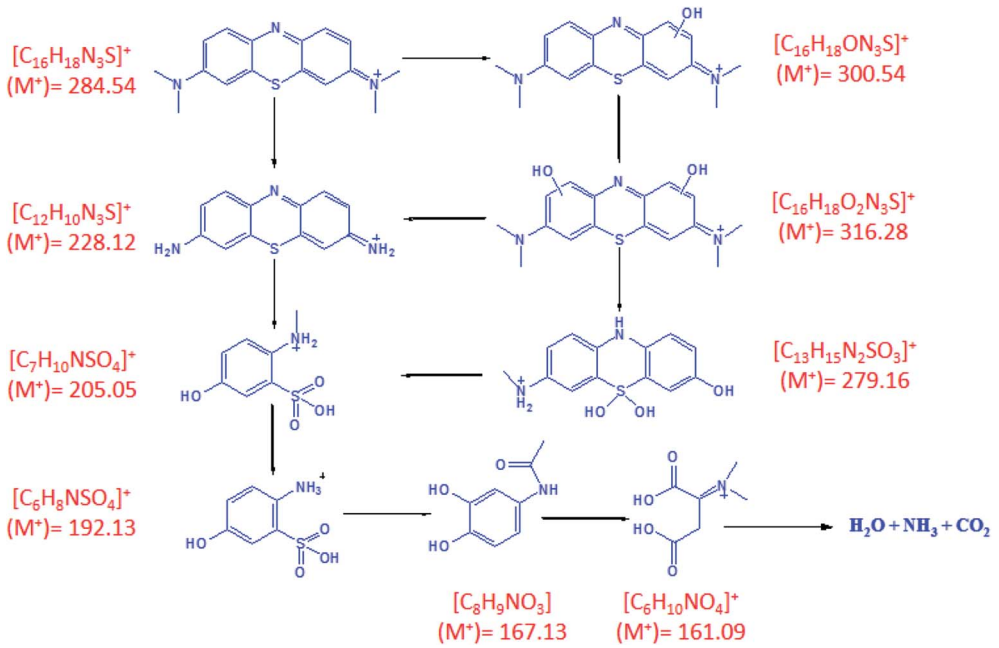

Fig. 8 Projected route for the photodegradation of the MB dye.

that the degradation efficiency of MB was ~88% after just 1.5 h over the surface of the $CuCrO_2$ nanoparticles in the presence of sunlight irradiation. This was found to be a significant enhancement in the photocatalytic efficiency of the $CuCrO_2$ nanoparticles compared to previous reports.[55,56] The kinetic plot was fitted by the pseudo-first-order rate equation using the rate constants of 0.0246 min^{-1}, and the R^2 value was found to be ~0.9830.

Fig. 7 shows the mass spectrum for the formation of the OH radical and the subsequent oxidation of MB dye after 60 minutes of sunlight irradiation. The signals at m/z = ~284, ~300, and ~316 of MB could be recognized on the basis of sequential hydroxylation of the molecule by the attack of the OH radical. However, other signals (m/z) could be due to the fragmentation of the dye molecule. The results are in good agreement with previous reports on the mineralization of the MB dye by the attack of free radicals.[57,58] Table 1 compiles the resulted fragmentations of the dye molecule with the m/z values after 60 minutes of irradiation. The reaction mechanism of the projected route for the photodegradation of the MB dye molecule over the surface of nanoparticles is shown in Fig. 8.[57–61] The most active bonds of the MB dye molecule are C–N and C–S, which can be easily broken by the attack of hydroxyl and superoxide free radicals to generate various fragments (oxidized organic molecules), followed by their transformation into inorganic substances such as CO_2, H_2O, SO_4^{2-}, NO_3^- *etc.*

4. Conclusions

The wide band gap $CuCrO_2$ nanoparticles with a delafossite structure were successfully synthesized by the polymeric citrate precursor method followed by heating at 900 °C in air. Phase purity, size, and shape of the $CuCrO_2$ nanoparticles were investigated by XRD and electron microscopy studies. The BET surface area of the $CuCrO_2$ nanoparticles (235 $m^2 g^{-1}$) was found to be more than 500 times that of bulk $CuCrO_2$. The dielectric loss and dielectric constant of the $CuCrO_2$ nanoparticles decreases with the increase in the frequency. $CuCrO_2$ nanoparticles possess optical transparency and a direct band gap energy of 77% and 3.09 eV, respectively, in the visible region. The $CuCrO_2$ nanoparticles also exhibit photoluminescence property at room temperature like other p-type TCOs, which can be utilized for practical applications such as in light-emitting diodes. A significant enhancement of the photocatalytic degradation of the organic pollutants (methylene blue) was studied over the surface of the $CuCrO_2$ nanoparticles for over 150 minutes. The photocatalytic degradation of the MB dye using the $CuCrO_2$ nanoparticles was further confirmed *via* mass spectrometry. The results suggested that the $CuCrO_2$ nanoparticles can be considered as one of the effective photocatalysts for the degradation of organic contaminants from water.

Acknowledgements

The authors thank Dr Sameer Sapra, IIT Delhi for fluorescence studies, CIF, Jamia Millia Islamia for X-ray diffraction studies, and AIIMS, New Delhi for electron microscopy studies. RP and MS thank UGC for research fellowships. The authors extend their sincere appreciation to the Deanship of Scientific Research at the King Saud University for funding this Research Group (RG-1435-007).

References

1 Y.-T. Nien, M.-R. Hu, T.-W. Chiu and J.-S. Chu, *Mater. Chem. Phys.*, 2016, **179**, 182–188.

2 D. Xiong, Z. Xu, X. Zeng, W. Zhang, W. Chen, X. Xu, M. Wang and Y.-B. Cheng, *J. Mater. Chem.*, 2012, **22**, 24760–24768.
3 G. A. Ozin, *Adv. Mater.*, 1992, **4**, 612–649.
4 B. K. Sonawane, M. P. Bhole and D. S. Patil, *Opt. Quantum Electron.*, 2009, **41**, 17–26.
5 S. H. Lim, S. Desu and A. C. Rastogi, *J. Phys. Chem. Solids*, 2008, **69**, 2047–2056.
6 G. Oskam and F. d. J. P. Poot, *J. Sol-Gel Sci. Technol.*, 2006, **37**, 157–160.
7 A. K. Rai, L. T. Anh, J. Gim, V. Mathew, J. Kang, B. J. Paul, J. Song and J. Kim, *Electrochim. Acta*, 2013, **90**, 112–118.
8 B. G. Lewis and D. C. Paine, *MRS Bull.*, 2000, **25**, 22–27.
9 T. Ahmad, S. Vaidya, N. Sarkar, S. Ghosh and A. K. Ganguli, *Nanotechnology*, 2006, **17**, 1236.
10 J. Krýsa, M. Keppert, J. r. Jirkovský, V. Štengl and J. Šubrt, *Mater. Chem. Phys.*, 2004, **86**, 333–339.
11 W. Yu-de, M. Chun-lai, S. Xiao-dan and L. Heng-de, *Nanotechnology*, 2002, **13**, 565.
12 S. Mori, S. Fukuda, S. Sumikura, Y. Takeda, Y. Tamaki, E. Suzuki and T. Abe, *J. Phys. Chem. C*, 2008, **112**, 16134–16139.
13 E. A. Gibson, A. L. Smeigh, L. Le Pleux, J. Fortage, G. Boschloo, E. Blart, Y. Pellegrin, F. Odobel, A. Hagfeldt and L. Hammarström, *Angew. Chem., Int. Ed.*, 2009, **48**, 4402–4405.
14 A. Nattestad, A. J. Mozer, M. K. R. Fischer, Y. B. Cheng, A. Mishra, P. Bauerle and U. Bach, *Nat. Mater.*, 2010, **9**, 31–35.
15 M. Yu, G. Natu, Z. Ji and Y. Wu, *J. Phys. Chem. Lett.*, 2012, **3**, 1074–1078.
16 J. Ahmed, C. K. Blakely, J. Prakash, S. R. Bruno, M. Yu, Y. Wu and V. V. Poltavets, *J. Alloys Compd.*, 2014, **591**, 275–279.
17 A. Nattestad, X. Zhang, U. Bach and Y.-B. Cheng, *J. Photonics Energy*, 2011, **1**, 011103–011109.
18 A. Renaud, B. Chavillon, L. Le Pleux, Y. Pellegrin, E. Blart, M. Boujtita, T. Pauporte, L. Cario, S. Jobic and F. Odobel, *J. Mater. Chem.*, 2012, **22**, 14353–14356.
19 A. Yella, H.-W. Lee, H. N. Tsao, C. Yi, A. K. Chandiran, M. K. Nazeeruddin, E. W.-G. Diau, C.-Y. Yeh, S. M. Zakeeruddin and M. Grätzel, *Science*, 2011, **334**, 629–634.
20 H. Kawazoe, M. Yasukawa, H. Hyodo, M. Kurita, H. Yanagi and H. Hosono, *Nature*, 1997, **389**, 939–942.
21 D. O. Scanlon and G. W. Watson, *J. Mater. Chem.*, 2011, **21**, 3655–3663.
22 K. Ueda, T. Hase, H. Yanagi, H. Kawazoe, H. Hosono, H. Ohta, M. Orita and M. Hirano, *J. Appl. Phys.*, 2001, **89**, 1790–1793.
23 Y. Wang, Y. Gu, T. Wang and W. Shi, *J. Alloys Compd.*, 2011, **509**, 5897–5902.
24 J. Tate, M. K. Jayaraj, A. D. Draeseke, T. Ulbrich, A. W. Sleight, K. A. Vanaja, R. Nagarajan, J. F. Wager and R. L. Hoffman, *Thin Solid Films*, 2002, **411**, 119–124.
25 K. Tonooka and N. Kikuchi, *Thin Solid Films*, 2006, **515**, 2415–2418.
26 S. Saadi, A. Bouguelia and M. Trari, *Sol. Energy*, 2006, **80**, 272–280.
27 W. Ketir, A. Bouguelia and M. Trari, *Water, Air, Soil Pollut.*, 2009, **199**, 115–122.
28 W. Ketir, A. Bouguelia and M. Trari, *Desalination*, 2009, **244**, 144–152.
29 W. Ketir, A. Bouguelia and M. Trari, *J. Hazard. Mater.*, 2008, **158**, 257–263.
30 N. Dupont, A. Kaddouri and P. Gélin, *J. Sol-Gel Sci. Technol.*, 2011, **58**, 302–306.
31 J. Ahmed, V. V. Poltavets, J. Prakash, S. M. Alshehri and T. Ahamad, *J. Alloys Compd.*, 2016, **688**, 1157–1161.
32 J. Ahmed and Y. Mao, in *Nanomaterials for Sustainable Energy*, American Chemical Society, 2015, ch. 4, vol. 1213, pp. 57–72.
33 J. Ahmed and Y. Mao, *J. Solid State Chem.*, 2016, **242**, 77–85.
34 X. Zhang, Y. Ding, H. Tang, X. Han, L. Zhu and N. Wang, *Chem. Eng. J.*, 2014, **236**, 251–262.
35 R. Srinivasan, B. Chavillon, C. Doussier-Brochard, L. Cario, M. Paris, E. Gautron, P. Deniard, F. Odobel and S. Jobic, *J. Mater. Chem.*, 2008, **18**, 5647–5653.
36 J. W. Lekse, M. K. Underwood, J. P. Lewis and C. Matranga, *J. Phys. Chem. C*, 2012, **116**, 1865–1872.
37 A. K. Ganguli, S. Vaidya and T. Ahmad, *Bull. Mater. Sci.*, 2008, **31**, 415–419.
38 A. Ganguly, T. Ahmad and A. K. Ganguli, *Langmuir*, 2010, **26**, 14901–14908.
39 T. Ahmad and I. H. Lone, *New J. Chem.*, 2016, **40**, 3216–3224.
40 T. Ahmad, I. H. Lone and M. Ubaidullah, *RSC Adv.*, 2015, **5**, 58065–58071.
41 V. Pocol, L. Patron, O. Carp, M. Brezeanu, E. Segal, N. Stanica and D. Crisan, *J. Therm. Anal. Calorim.*, 1999, **55**, 143–154.
42 A. Gil, S. A. Korili and G. Y. Cherkashinin, *J. Colloid Interface Sci.*, 2003, **262**, 603–607.
43 M. Ubaidullah, I. H. Lone, O. A. Al-Hartomy, D. Kumar and T. Ahmad, *Adv. Sci. Lett.*, 2014, **20**, 1354–1359.
44 B. K. Bammannavar, L. R. Naik and B. K. Chougule, *J. Appl. Phys.*, 2008, **104**, 064123.
45 C. G. Koops, *Phys. Rev.*, 1951, **83**, 121–124.
46 A. Jacob, C. Parent, P. Boutinaud, G. Le Flem, J. P. Doumerc, A. Ammar, M. Elazhari and M. Elaatmani, *Solid State Commun.*, 1997, **103**, 529–532.
47 P. Boutinaud, D. Garcia, C. Parent, M. Faucher and G. Le Flem, *J. Phys. Chem. Solids*, 1995, **56**, 1147–1154.
48 A. C. Rastogi, S. H. Lim and S. B. Desu, *J. Appl. Phys.*, 2008, **104**, 023712.
49 R. D. Shannon, D. B. Rogers, C. T. Prewitt and J. L. Gillson, *Inorg. Chem.*, 1971, **10**, 723–727.
50 H.-Y. Chen and K.-P. Chang, *ECS J. Solid State Sci. Technol.*, 2013, **2**, P76–P80.
51 T. S. Tripathi, J.-P. Niemela and M. Karppinen, *J. Mater. Chem. C*, 2015, **3**, 8364–8371.
52 S. Götzendörfer, C. Polenzky, S. Ulrich and P. Löbmann, *Thin Solid Films*, 2009, **518**, 1153–1156.
53 J. Tauc, *Mater. Res. Bull.*, 1968, **3**, 37–46.
54 A. Ibrahim and S. K. J. Al-Ani, *Czech J. Phys.*, 1994, **44**, 785–797.
55 D. Xiong, H. Chang, Q. Zhang, S. Tian, B. Liu and X. Zhao, *Appl. Surf. Sci.*, 2015, **347**, 747–754.

56 S. Chin, E. Park, M. Kim and J. Jurng, *Powder Technol.*, 2010, **201**, 171–176.
57 H. W. P. Carvalho, A. P. L. Batista, P. Hammer and T. C. Ramalho, *J. Hazard. Mater.*, 2010, **184**, 273–280.
58 F. Huang, L. Chen, H. Wang and Z. Yan, *Chem. Eng. J.*, 2010, **162**, 250–256.
59 A. Houas, H. Lachheb, M. Ksibi, E. Elaloui, C. Guillard and J.-M. Herrmann, *Appl. Catal., B*, 2001, **31**, 145–157.
60 J.-E. Lee, N. T. Khoa, S. W. Kim, E. J. Kim and S. H. Hahn, *Mater. Chem. Phys.*, 2015, **164**, 29–35.
61 H.-P. Jing, C.-C. Wang, Y.-W. Zhang, P. Wang and R. Li, *RSC Adv.*, 2014, **4**, 54454–54462.